Improved low-energy diffuse scattering electron-spin polarization analyzer

M. R. Scheinfein, D. T. Pierce, J. Unguris, J. J. McClelland, R. J. Celotta,
and M. H. Kelley

National Bureau of Standards, Gaithersburg, Maryland 20899

(Received 1 August 1988; accepted for publication 11 September 1988)

An improved low-energy diffuse scattering electron-spin polarization analyzer is described. It is based on the low-energy (150 eV) diffuse scattering of polarized electrons from polycrystalline evaporated Au targets. By collecting large solid angles and efficiently energy filtering the scattered electrons, a maximum figure of merit, FOM $= S^2 I/I_0 = 2.3 \times 10^{-4}$ is achieved. Maximum measured values of the Sherman function were $S = 0.15$. Further, the instrumental (false) asymmetry due to changes in the trajectory of the incident electron beam has been minimized by balancing the angular and displacement asymmetries. A total residual scan asymmetry as low as 0.0035/mm has been measured over 4-mm scan fields at the Au target in the detector. This instrumental asymmetry would produce a maximum error in the polarization in a SEMPA experiment of less than 0.3% for a 100-μm full-field scan. Details of the design and performance of the new detector are given.

INTRODUCTION

Electron-spin polarization measurements have many important technological applications. As magnetic device densities increase, important new diagnostic techniques are being developed to characterize and analyze the new structures and fabrication techniques. One such technique, scanning electron microscopy with polarization analysis (SEMPA), utilizes the property that secondary electrons excited by a fast electron beam incident on a ferromagnetic specimen retain their spin when escaping from the specimen surface.[1,2] Measurement of the components of the spin vector can be directly related to the magnetization of the sample. Basic studies of the onset of magnetism and of domain-wall dynamics are also looking towards polarized electron spectroscopy as a means of gaining physical insight.

The polarization of an electron beam is the ensemble average of the expectation value of the Pauli spin operator. The statistical description of a mixture of spin states of a polarized beam is appropriately described in the density matrix formalism.[3] More simply, the polarization P is given by

$$P = \frac{N_\uparrow - N_\downarrow}{N_\uparrow + N_\downarrow}, \tag{1}$$

where $N_\uparrow$ and $N_\downarrow$ are the number of electrons with spins parallel (↑) or antiparallel (↓) to some quantization axis. The degree of polarization has a range of $-1.0 \leqslant P \leqslant 1.0$. In a spin polarization detector, a mechanism for separating the spins is provided, usually utilizing the left/right scattering asymmetry resulting from the spin-orbit coupling in high-angle collisions with heavy atoms.

The high-energy (conventional) Mott analyzer[4] has been widely used to measure electron-spin polarization. This analyzer utilizes scattering asymmetry resulting from spin-orbit coupling in the high-energy ($E \geqslant 100$ keV) electrons scattering from heavy metal (usually Au) foils. The sensitivity of the analyzer to the beam polarization is characterized by its Sherman function S. The effective Sherman function is a measure of the scattering asymmetry in the detector averaged over the collection solid angles. We will use the notion of the effective Sherman function as applied to the scattering asymmetry in a detector interchangeably with the strict definition of the Sherman function, which depends upon the scattering angle. The scattering asymmetry resulting from the interaction of fast polarized electrons with thin Au foils has been calculated[5,6] and measured[4] for a wide variety of both scattering angles and incident electron energies. In a typical Mott detector, the scattered electrons are detected by two apertures located at polar scattering angles of 120° with respect to the incident beam (30° above the Au film plane) and oriented opposite each other, e.g., at azimuth angles of 0° and 180°, respectively. Mott detectors have typical Sherman functions from 0.20 to a maximum of 0.39. The figure of merit (FOM) for a polarimeter is defined as[3]

$$\text{FOM} = S^2 I/I_0, \tag{2}$$

where S is the Sherman function, I is the sum of the current detected by the two opposite detectors, and I_0 is the incident beam current. The FOM for a fully optimized Mott detector can be as high as 1×10^{-4}. The signal-to-noise figure for a polarization detector is related to its figure of merit.[3] The higher the FOM, the better the signal-to-noise for a given polarization measurement.

Improvements to the traditional Mott analyzer have been made[7] and new detectors with reduced beam energies 20–30 keV have been produced.[8,9] These detectors have Sherman functions of approximately $0.13 \rightarrow 0.30$ and a FOM of up to 2×10^{-5}. When the target is a single crystal instead of an amorphous or polycrystalline film, the left/right asymmetry due to spin-orbit scattering is present in the diffracted beams, and a detector based on this principle has been developed.[10,11] In this polarized low-energy electron diffraction (PLEED) detector, a beam of low-energy electrons is diffracted from the W(001) surface and the $(\bar{2},0)$ and the $(2,0)$ diffracted beams are detected. A Sherman function of

$S = 0.27$ and a figure of merit of $\mathrm{FOM} = 1.6\times 10^{-4}$ results. Other techniques, such as the absorbed current detector[12] and low-energy scattering from a metal-atom beam (such as Hg),[13] have been utilized to measure electron polarization. Comparisons of various polarimeters can be found in the literature.[14,15]

The low-energy diffuse scattering spin polarization electron detector[14] also relies on the spin-orbit interaction to produce a left/right asymmetry. This detector consists of an evaporated gold target, retarding grids, and channel plates. It relies on large collection solid angles to increase the performance of the detector. We will discuss the design and optimization of this detector.

I. ANALYZER DESIGN CONSIDERATIONS

A. Design objectives

The starting point for the present polarimeter design was the diffuse scattering low-energy spin polarization detector described in detail by Unguris *et al.*[14] We would like to implement an additional design constraint, so that the instrumental asymmetry be minimized. All other initial design criteria also have been implemented in this design. These requirements are small physical detector size, high efficiency as determined by the figure of merit S^2I/I_0, the largest possible Sherman function S, as large an acceptance phase space as possible consistent with the low-energy nature of the detector, and ultrahigh-vacuum components throughout. The scattering film in the detector is evaporated Au, which stays clean and is easily evaporated. The incident beam energy into the detector is optimally 150 eV. Although it may be preferable, electron-optically, to operate at higher beam energies, the Sherman function for Au exhibits a local maximum at 150 eV.

Since minimizing the instrumental asymmetry was the impetus for redesigning the detector, it will be discussed first. Next, a discussion of the optimization of the Sherman function and the FOM will follow. Finally, a discussion of the measurements of the detector performance will be given.

B. Instrumental asymmetry

All of the polarization detectors discussed in the Introduction (including this detector) rely on the left/right scattering asymmetry due to spin-orbit coupling to determine the unknown beam spin polarization in the event that the incident beam polarization cannot be modulated. In this sense, all of the detectors are position-sensitive detectors. To measure the spin, a difference in the scattering between two channels is required, implying that stringent geometrical constraints must be satisfied. In situations where exacting design tolerances are not met, or precise beam alignment and positioning cannot be guaranteed, an instrumental or false asymmetry will occur. Any effect that introduces spurious signals systematically into either the left or right channel introduces a false asymmetry into a detector based on a left/right scattering asymmetry.[3,4,16] To characterize the instrumental asymmetry A_I, we wish to determine the total number of electrons reaching each "channel" (left or right scattering detector aperture) of the detector for a given beam alignment condition.

A schematic cross section of a polarization detector based on the principles described above is shown in Fig. 1. A detector consists of left and right channels, labeled L and R. There are two detectors shown in the figure differing only in an overall scale constant where the first detector consisting of L and R channels is in close proximity to the Au foil, and the second detector also consisting of L and R channels is further from the Au foil. Assume that the out-of-plane angles are identical to the in-plane angles, in other words, the detector cross section could be that of a conventional Mott analyzer with circular acceptance apertures into the L and R electron counters. The smaller detector is labeled with a "1," while the larger detector is labeled "2." As indicated in the figure, both of the detectors subtend the same solid angle at the Au target, and thus both detectors have the same collection efficiency and must therefore have the same figure of merit. Further, both of the detectors have the same average scattering angle corresponding to the central axis of the detector, denoted by θ_0, and the same inner and outer scattering angles, θ_{in} and θ_{out}. The coordinates of the intersection of the central axis with the detector planes for the two detectors are different, and are denoted by $\pm\bar{x}_{1(2)},\bar{z}_{1(2)}$.

For an unpolarized incident electron beam, the number of electrons collected in channels L and R is given by

$$I_i = \int_{\mathrm{det}_i} \frac{d\sigma(\theta,\phi)}{d\Omega}\, d\Omega_i, \qquad (3)$$

where I_i is the current measured by channel i (i represents either L or R), $d\sigma(\theta,\phi)/d\Omega$ is the different cross section for the scattering process, and Ω_i is the solid angle subtended by channel i. The instrumental asymmetry associated with this configuration is

$$A_I = \frac{I_L - I_R}{I_L + I_R}. \qquad (4)$$

If the beam moves or tilts on the scattering target, an instrumental asymmetry A_I will result from changes in the solid angle Ω and changes in the relative cross section $\sigma_i(\theta,\phi)$

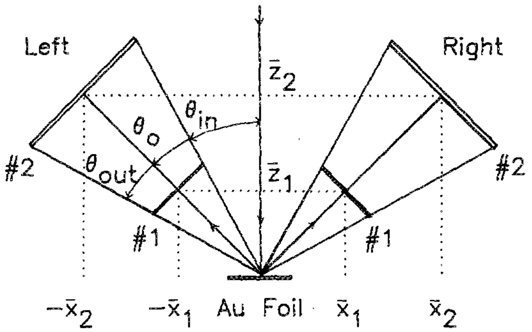

FIG. 1. Two generic polarization detectors #1 and #2 with position centroids $\pm\bar{x}_{1,2}$ and $\bar{z}_{1,2}$, angle centroid θ_0, and inner and outer angles θ_{in} and θ_{out} are shown. The out-of-plane angular extent of the detection channels R and L are identical to the in-plane angles.

subtended by each channel *i*. Consider these effects for the two detectors proposed in Fig. 1.

Figure 2(a) depicts a pure displacement Δ of the beam at the Au foil. This displacement normalized to the detector geometry is arbitrary, and $\Delta/\bar{x}_1 = \Delta/\bar{z}_1 = 0.27$ and $\Delta/\bar{x}_2 = \Delta/\bar{z}_2 = 0.135$. The bundles of rays indicated are subtended by the two detectors. It is clear now that the two detectors are no longer identical. The relative change in the angles subtended by the two detectors due to displacement Δ is summarized in Table I.

Without considering the relative change in the cross section for the two detectors, it is evident that detector 1, the smaller of the two, suffers from the larger instrumental asymmetry. As the beam moves towards a channel of the detector, as in this case towards the *R* channel, that channel receives more electrons due to the solid angle subtended; the other channel, the *L* one in this case, receives less, yielding a positive A_I.

Figure 2(b) depicts a pure angular deviation $\Delta\theta$. As can be seen, there is no change in solid angle due to a pure tilt.

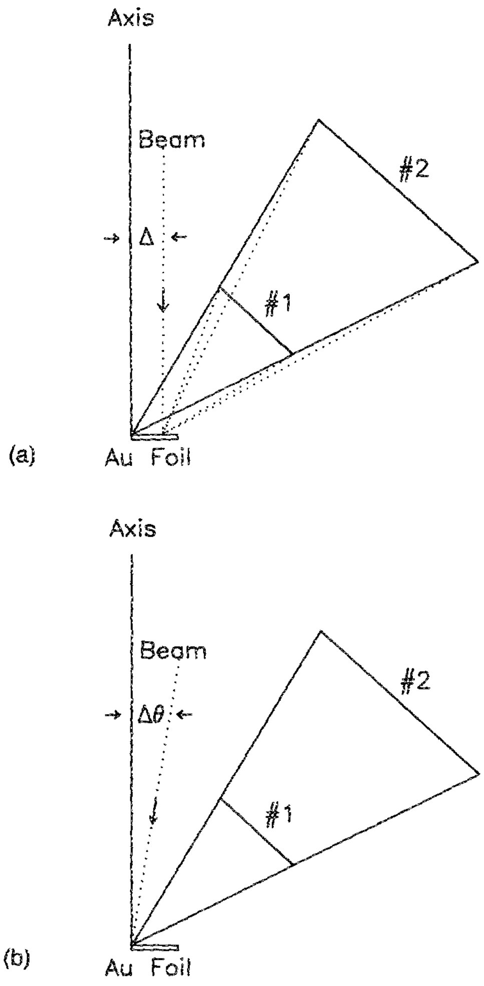

FIG. 2. (a) Difference in solid angles subtended by detectors #1 and #2 due to the displacement Δ illustrates the effect that detector size has in determining the displacement instrumental asymmetry. (b) Solid angles subtended by detectors #1 and #2 are identical for angular displacements $\Delta\theta$, but an angular instrumental asymmetry results from the angular dependence of the cross section.

TABLE I. Comparison of misalignment tolerances for the detector of Fig. 2. Detector 1 has a normalized position misalignment $\Delta/\bar{x}_1 = \Delta/\bar{z}_1 = 0.27$, while detector 2 has a normalized position misalignment $\Delta/\bar{x}_2 = \Delta/\bar{z}_2 = 0.135$.

Detector	θ_0	$\theta_{\rm in}$	$\theta_{\rm out}$	$\Omega(\rm rad^2)$	$\Delta\Omega/\Omega$
Aligned	45°	29°	61°	0.93	0.00
1	37°	19°	56°	1.24	0.33
2	42°	25°	59°	1.05	0.13

However, when the angular dependence of the cross section is taken into account, an angular instrumental asymmetry results. The cross section has a functional θ-dependence, which in this case exhibits a strong enhancement in the backscattered direction. Thus, although both detectors 1 and 2 have the same angular asymmetry A_θ, this asymmetry is nonzero, for in this case the *R* detector collects more electrons than the *L* detector due to the angular dependence of $\sigma(\theta)$.

Consider the cross section and top views of the diffuse low-energy scattering spin polarization detector shown in Fig. 3. The azimuthal angles (ϕ) are depicted in the end view insert, and the scattering angles (θ) are depicted in the cross-sectional view. To determine the asymmetry as a function of off-axis position and slope, we express the incremental solid angle into the quadrants as $d\Omega = (\hat{n}\cdot\mathbf{R})dA/R^3$, where dA is the incremental surface area of the first grid G_1, $\hat{n}$ is the normal to the first grid, R is the distance from the scatterer to the increment of surface area, and h is the distance in the vertical direction of the drift space. Referring to Fig. 3, and positioning the incident beam pencil at (x',y'), the collected intensities on the opposite quadrants *A* and *C* are

$$I_{A,C} = I_0 \int_{\text{detector}A,C} \frac{\sigma(\theta,\phi)\cos(\theta)}{[(x \mp x')^2 + (y \mp y')^2 + h^2]}\, dA, \tag{5}$$

where the ($-$) goes with detector *A* and the ($+$) goes with detector *C*. Since the system is cylindrically symmetric, the

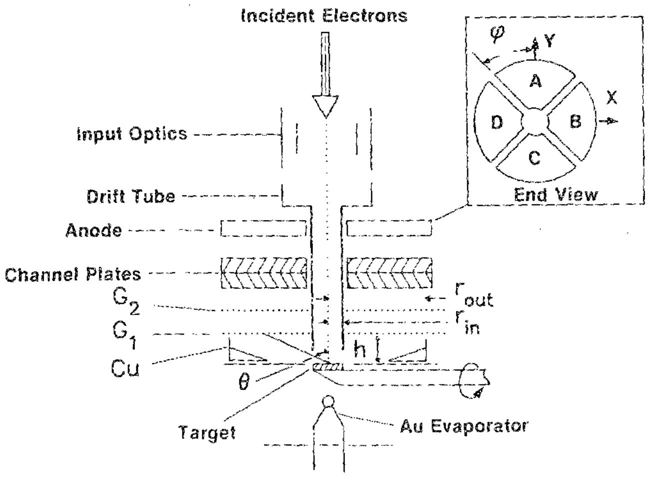

FIG. 3. Cross-sectional view of the low-energy diffuse scattering spin polarization detector with an end view of the anode as seen from the Au foil.

ϕ-dependence can be eliminated in the cross section. Denoting the inner detector collection radius by $r_{\rm in}$ and the outer detector collection radius by $r_{\rm out}$ (as defined in Fig. 3), the intensities are given by

$$I_{A,C} = \int_0^{r_{\rm in}} dy^\dagger \int_{\sqrt{r_{\rm in}^2 - y^{\dagger 2}}}^{\sqrt{r_{\rm out}^2 - y^{\dagger 2}}} dx^\dagger \times \frac{\sigma(\theta')\cos(\theta')}{[(x^\dagger \mp x')^2 + (y^\dagger \mp y')^2 + h^2]} + \int_{r_{\rm in}}^{r_{\rm out}} dy^\dagger \int_0^{\sqrt{r_{\rm out}^2 - y^{\dagger 2}}} dx^\dagger \times \frac{\sigma(\theta')\cos(\theta')}{[(x^\dagger \mp x')^2 + (y^\dagger \mp y')^2 + h^2]}, \tag{6}$$

where

$$\theta' = \arctan \frac{\sqrt{(x^\dagger \mp x')^2 + (y^\dagger \mp y')^2 + h^2}}{h}, \tag{7}$$

and the integration variables $x^\dagger$ and $y^\dagger$ are a Cartesian coordinate system rotated by 45° with respect to the x–y axis of Fig. 3. In this way, the $x^\dagger$–$y^\dagger$ axis is aligned with the gaps between the channel plate quadrants greatly facilitating the evaluation of the intensity integrals. θ' is the angle that the beam incident on x'–y' and scattered to position $x^\dagger$–$y^\dagger$ on the first grid makes with the Au film normal. Displayed in Fig. 4 is an asymmetry map for the old detector where contours of constant asymmetry due to position displacement are indicated in percent. Pure displacement of the incident beam causes large false asymmetries. The angular asymmetry can be determined by replacing θ in the previous equation by $(\theta - \xi)$, where ξ is the tilt along the projection bisecting the detector A–C symmetry axis.

For the detector pair A–C, displacement of the incident beam perpendicular to the $\hat{y}$-axis should not introduce any instrumental asymmetry. Likewise, any tilt in a $y =$ constant plane should not introduce any instrumental asymmetry into the A–C pair. In Fig. 4, an asymmetry map for the original diffuse scattering spin polarized electron detector[14] is shown. The asymmetry is linear in displacement as the beam is moved along the $\hat{y}$-axis. As is evident, the displacement asymmetry is significant, which led us to the current redesign effort. For this calculation, low-energy electron-scattering cross sections[17–19] corrected for solid substrate effects[20] were used.

The instrumental asymmetry arises thus from a mix of the changing cross section and solid angles subtended by the opposing quadrants. The angular asymmetry is entirely due to cross-section effects, while displacement asymmetry is dominated by solid angle effects. This, of course, does not include any additional asymmetries that may arise from channel plate gain or amplifier gain imbalances and counting electronics differences.

In general, the instrumental asymmetry due to displacement can be minimized by making the detector larger as the trend in Table I indicates. Effectively, an infinitely large detector infinitely far away has no displacement asymmetry.

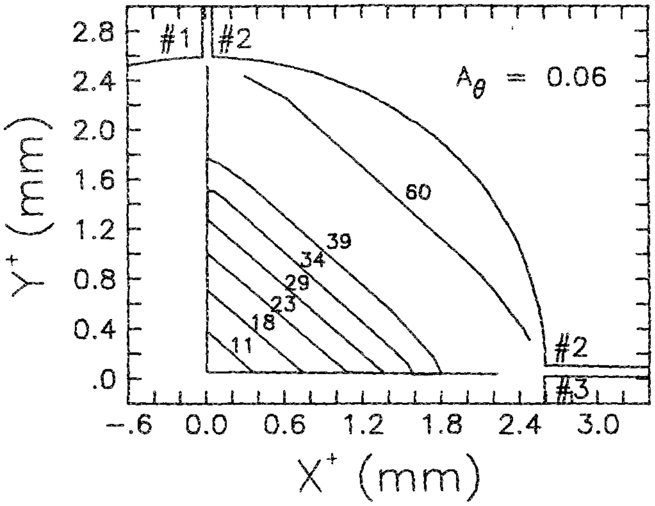

FIG. 4. Asymmetry contour map for the low-energy diffuse scattering spin polarization detector where the angular asymmetry is $A_\theta = 6\%$ per degree and the percentage asymmetry is shown for contours of displacement. The asymmetry is measured between quadrants #2 and #4 (not shown). Motion along the $X^\dagger$ -- $Y^\dagger$ introduces no false asymmetry into quadrants #1 and #3.

To proceed to minimize these aberrations, a detector with as large an electron-optical size as possible should be designed consistent with all of the other design requirements. For several applications, including the SEMPA experiment, physically large detectors may significantly decrease the performance of the total system by introducing, for example, vibrations and mechanical instabilities into the SEMPA experiment or preclude the movement of the detector in, for example, an angle-resolved photoemission measurement. Thus, it is advantageous for the detector to be electron-optically large, yet still physically small.

To illustrate some of the relevant characteristics of instrumental asymmetry as it relates to size, we refer to Table II. Listed for comparison are the position centroids (refer to Fig. 1) $\bar{x}$ and $\bar{z}$, angular centroid θ_0, inner and outer angles, $\theta_{\rm in}$ and $\theta_{\rm out}$, and the approximate displacement and angular instrumental asymmetries A_D and A_θ for some polarimeters.

Low-energy electron cross sections were used for the low-energy diffuse scattering spin polarimeters, while Mott cross sections[22] were used to calculate the Mott type detector asymmetries. The details of the new detector will be given in Sec. III.

C. Instrumental asymmetry compensation

Since all of the spin-polarization analyzers appear to have non-negligible instrumental asymmetries in the smal

TABLE II. Comparison of detector instrumental asymmetries for variou polarimeters.

Detector	$\bar{x}$	$\bar{z}$	θ_0	$\theta_{\rm in}$	$\theta_{\rm out}$	A_D (%/mm)	A_θ (%/deg
Ref. 21	26.7	13.6	63°	43°	83°	6.1	2.0
Ref. 7	29.4	17.0	60°	54°	66°	5.5	2.0
Ref. 8	14.0	8.5	59°	49°	69°	13.9	2.1
Ref. 14	3.7	3.7	45°	30°	60°	28.0	6.0
This work	12.8	11.2	49°	30°	68°	6.0	6.0

detector size regime, some careful electron optical design is required to further reduce this deleterious effect. Consider the schematic depiction of a detector and the ray path in Fig. 5.

This is a generic spin polarization detector. The incident electron ray paths are shown off-axis and tilted. The ray is displaced towards the R channel, yet it is tilted toward the L channel. Qualitatively, in this regime, the R channel receives more electrons due to the displacement and the enhanced solid angle, but yet it receives fewer electrons due to the tilt and the decrease in $d\sigma(\theta)/d\theta$. Similarly, the L channel receives more electrons due to the tilt yet fewer due to the displacement. If the asymmetry due to displacement can exactly balance that asymmetry due to angle for a given set of input conditions, then the total instrumental asymmetry A_I can be markedly reduced.[23] To meet these conditions, the following criteria must be met[3,4,16]

$$\int_{\mathrm{channel}(\Delta\theta)} \frac{d\sigma(\theta)}{d\Omega}\, d\Omega = f(\Delta\theta), \qquad (8)$$

or the integral of the cross section over the detector must be a function of the misalignment angle $\Delta\theta$, and

$$\int_{\mathrm{channel}(\Delta)} \frac{d\sigma(\theta)}{d\Omega}\, d\Omega = g(\Delta). \qquad (9)$$

The integral of the cross section over the detector must also be a function of the displacement misalignment Δ. What is essential for compensation is that the angular and displacement asymmetries are equal and opposite. We find that the functional dependence of the above integrals is linear, although linearity is not essential. Since the asymmetries are linear in displacement and angles, we can balance them against each other using the first order real imaging properties of electron lenses on the input to the detector. Note that the displacement misalignment integral is dominated by changes in the solid angle.

If these (linear) relationships can be satisfied, then a set of (linear) equations in misalignment angle $\Delta\theta$ and misalignment displacement Δ can be solved to yield zero instrumental asymmetry for known detector displacement A_D and angular A_θ asymmetries. This is driven by the fact that most physical designs automatically constrain the likely displacements and enforce some kind of correlation between the displacements and angles at the detector target foil. We wish to exploit this correlation.

It is useful to describe this problem in a more general way using the phase space formalism. The compensation condition implies that a linear relationship exists between the tilt and displacement of the beam at the Au foil. In phase space (the $[\hat{r}-\hat{\theta}]$ space where now there are actually two separate phase space projections onto the $[\hat{x}-\hat{\theta}_x]$ and $[\hat{y}-\hat{\theta}_y]$ subspaces applicable to detecting the two different transverse components of the spin polarization vector), the compensation condition corresponds to a straight line. Consider the variety of mappings shown in Fig. 6. The final phase space at the detector is shown in Fig. 6(a) as a straight line of some slope corresponding to the compensation condition. Consider an experiment where the beam is largely parallel, yet it moves around such as in a photoexcitation process by a parallel x-ray beam where the beam is not totally stationary. This condition corresponds to the input phase space of Fig. 6(b), which must be mapped through an appro-

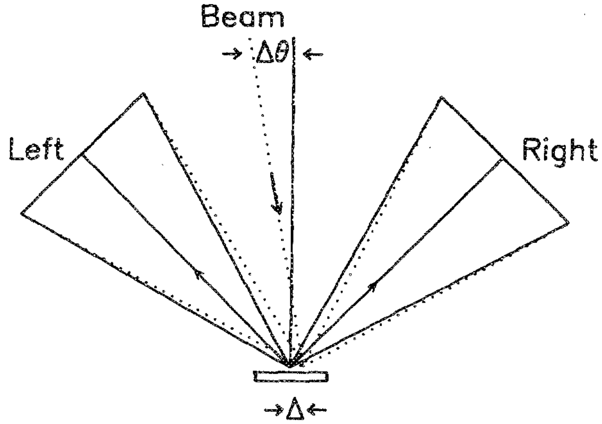

FIG. 5. Instrumental asymmetry compensation scheme where the angular and displacement asymmetries are balanced against one another to yield zero total asymmetry.

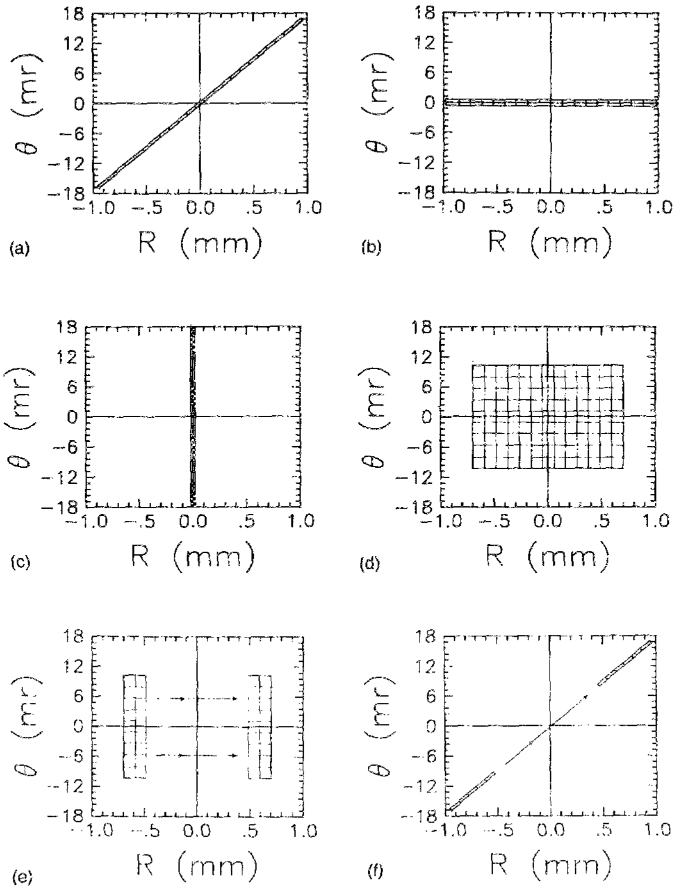

FIG. 6. (a) Detector phase space mapping for a compensated detector. (b) Input phase space for a beam fixed in angle yet moving in position. (c) Input phase space for a beam fixed in position yet moving in angle. (d) Input phase space for the SEMPA experiment where the beam is scanned and finite angles are accepted into the optics. (e) General input phase space indicating scanned beam movement. (f) Detector phase space of input (e) indicating scanned beam movement.

priate set of transport optics to the detector phase space of Fig. 6(a). Similarly, the experiment in Fig. 6(c) is that of a focused beam, which is fixed in position, yet is rocking in angle such as would be produced in an electron diffraction experiment. This input phase space must therefore be mapped by some transport optics to the detector phase space of Fig. 6(a). In Fig. 6(d), the input phase space of the SEMPA experiment[1,2] is shown. This corresponds to collecting a beam of finite angular extent that is being rastered in position over the sample. This too must be mapped to the appropriate detector-compensated phase space. Essentially, one must design appropriate transport optics to couple the phase space of the experiment to the detector carefully to compensate the instrumental asymmetry fully. The essential elements of the design are elucidated in Figs. 6(e) and 6(f). As the input phase space of Fig. 6(e) is scanned, a finite angular bundle of rays is moved in position. This must be mapped into the detector phase space of Fig. 6(f). Notice that the movement in position r must be mapped to positions along the compensation line, thus as the phase space of Fig. 6(e) is scanned from left to right, the phase space of Fig. 6(f) is scanned from bottom left to top right.

D. Azimuthal angle scattering design considerations

The previous version of the low-energy diffuse scattering electron-spin polarization analyzer[14] utilized four quadrants for the detection of the two transverse spin components. Referring to Fig. 3, the $\hat{x}$ polarization

$$P_x = \frac{1}{S}\frac{N_C - N_A}{N_C + N_A}, \tag{10}$$

and the $\hat{y}$ polarization

$$P_y = \frac{1}{S}\frac{N_B - N_D}{N_B + N_D} \tag{11}$$

are defined by the appropriate scattering asymmetries divided by the Sherman function S for the detector. Consider the measurement of only the $\hat{x}$ component of the polarization by detectors A and C. Further, assume that the sectors of the anode may have an arbitrary half-angle ϕ, where ϕ for the case of Fig. 3 is 45°.

We would like to investigate the possibility of improving the detector performance by increasing the number of sectors on the anode. Assume that the beam of polarized electrons strikes the detector Au foil uniformly distributed in azimuthal scattering angle, such as the situation that would result from a SEMPA experiment where a point source of secondaries is imaged onto the detector foil. Assume that the scattering from the foil for an unpolarized beam is uniform such that $dI = \eta I_0 d\phi$, where η is the elastic backscattering coefficient (at some fixed polar angle—θ). Further, the form for the current measured at the detectors of Sherman function S and beam polarization P is[3,11]

$$dI_{A,C} = \eta I_0 [1 \mp PS\cos(\phi)]\, d\phi. \tag{12}$$

To determine the performance, one calculates the asymmetry function $(N_C - N_A)/(N_C + N_A)$ and then forms the figure of merit as a function of the integrated azimuth angle ϕ. This yields a function of the form

$$\mathrm{FOM}(\phi) = \eta S^2 P^2 [\sin(\phi)]^2/\phi. \tag{13}$$

This function increases to a maximum near 67°. The value of this function is identical for $\phi = 45°$ and 90°. Also, the peak value of the FOM for the 67° sectors rises by only 18% over the value of a quadrant ($\phi = 45°$) detector. This moderate rise in efficiency in our estimation did not warrant moving into an eight-segment detector and forming sums and differences of the various sectors to determine the polarization.

E. Polar angle scattering design considerations

The FOM of a spin-polarization detector can be improved by increasing the effective Sherman function or by increasing the angular collection efficiency. Clearly, these aims must be consistent in the sense that a large increase in the collection efficiency I/I_0 must not degrade the Sherman function such that the FOM actually decreases, or a large increase in the Sherman function must not limit the collection efficiency so as to decrease the FOM. Of the detectors surveyed in the introduction, the PLEED detector, the Hg-beam detector, and the conventional Mott detector have moderate Sherman functions and low current collection efficiencies. The lower-energy Mott detectors and the low-energy diffuse scattering detector have somewhat lower Sherman functions, yet display a much-improved current collection efficiency.

The first design issue involves the optimum integrated polar angles for the low-energy diffuse scattering detector. In the previous design,[14] the inner angle θ_{in} and outer angle θ_{out} (as defined by Fig. 1) were 30° and 60° for normal operation. We calculated the optimum collection angles. Low-energy elastic scattering cross sections for polarized electron scattering corrected for finite substrate effects[17-20] were integrated appropriately to determine the FOM as a function of θ_{in} and θ_{out}. It was determined that, for $\theta_{\mathrm{out}} > 60°$, the optimum θ_{min} was about 30°. Further, as the outer collection angle increased to near $\theta_{\mathrm{out}} = 70°$, the FOM increased, leveling off somewhat for $\theta_{\mathrm{out}} > 70°$. Thus, to maximize the FOM of the detector, we set out to collect electrons scattered from the Au target between $30° \leqslant \theta \leqslant 70°$.

In the previous design,[14] the electrons were incident on the Au foil in a field-free region. After scattering, the electrons drifted towards grid 1 (G_1). After passing through G_1, a retarding grid, grid 2 (G_2), energy selected the scattered electrons. The previous configuration suffers from the problem that energy filtering is a function of the polar angle. A retarding grid analyzer of this type is a momentum analyzer, and it really measures the velocity component perpendicular to the grids. The component of the velocity perpendicular to the grids is $v_z = \sqrt{2E_{\mathrm{scattered}}/m_e}\cos(\theta)$. To eliminate this problem, include a field-shaping electrode within the detector to shape the electron trajectories in the intergrid region such that they are incident normally onto G_1, and achieve better energy filtering of the scattered electrons.

II. ANALYZER DESIGN IMPLEMENTATION

Figure 7 is a cross section of the new detector with the trajectories of elastically scattered 150 eV electrons. For these calculations, the bias on the Cu electrode is − 150 V, and the bias on the first grid G_1 is 0 V. The detector length in z has been increased from 5 to 22.5 mm, but the radial extent of the detector remains the same as in the previous design. The design was constrained not to increase the radial dimensions due to practical engineering considerations involved with the channel plates and the grids. The length was increased to decrease the displacement instrumental asymmetry. The length was constrained by forcing the angular and displacement instrumental asymmetries to be equal for 1-mm-maximum displacements and 1° maximum tilts. This is consistent with other electron optical constraints imposed by the transport optics. Further, the physical size of the detector remains small.

A drift tube extends down through the grids to within 5 mm of the Au foil. The drift tube serves several purposes: (1) to allow a drift region for the incident electron trajectories; (2) to define the inner collection angle $\theta_{\text{in}} = 30°$; (3) to prevent electrons deflected back by the negative potential on the shaped Cu electrode from being collected at a quadrant on the opposite side of the detector; and (4) to aid in defining the field needed for effective energy filtering.The grid structure (G_1 and G_2) and the front of the first channel plate as shown are unchanged from the previous design. A shaped Cu electrode has been inserted. The Cu electrode serves several purposes: (1) to shape the field such that the electrons trajectories are more normal to G_1 for improved energy filtering in the grids; and (2) to deflect wide-angle scattered electrons back towards the detector thereby increasing the effective electron optical size of the detector, more than doubling the effective radius of the channel plates.

To determine the performance of new designs, detector electrode configurations were simulated. Laplace's equation was solved for the cylindrically symmetric structure by the charge density method, whereby the conductor surfaces are suitably sectioned and the surface charge density determined such that the potential boundary conditions are met.[24,25] Once the surface charge densities on all of the conductors is known, a fourth-order Adams–Bashforth/Adams–Moulton predictor–corrector ray-tracing algorithm traced the electrons through the detector where the electric field components are calculated to all orders from the charge density distribution. In this way, the performance of the new detector could be predicted.

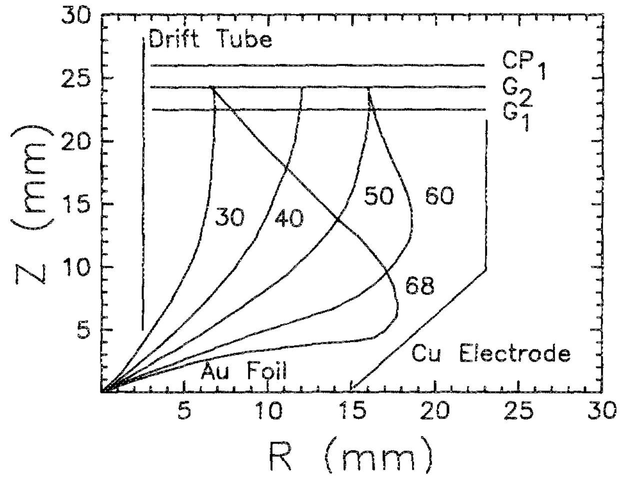

FIG. 7. Cross section of new detector. Elastically scattered 150 eV electron trajectories are shown with their takeoff angles in degrees.

For the current design, the electron trajectories are directed more normal to G_1. The results are summarized by looking at the z-component of the electron kinetic energy E_z at G_1 as a function of takeoff angle from the foil in Table III. Here, the final electron kinetic energy along the $\hat{z}$-direction, E_z, is given for elastically scattered electrons of 150 eV initial energy. For comparison with the previous design, this simulation biased the drift tube, G_1, and the Au foil at ground potential. The potential on G_2 is − 40 V, and the potential on the shaped Cu electrode is − 150 V.

The results of Table III indicate that the energy window allowed into the detector is much more tightly controlled in the new design. The new design has a much more uniform energy filtering function as a function of polar scattering angle.

III. DETECTOR PERFORMANCE

A. Figure of merit and Sherman function

We constructed a prototype of the new polarization detector. A series of measurements of the normalized current I/I_0 and the Sherman function S were performed for a wide variety of bias potentials on G_1, G_2, and on the shaped Cu electrode to be referred to as *Cu*.

The current I/I_0 was measured by providing a beam of 150 eV electrons incident on the Au foil from a standard low-energy electron diffraction (LEED) gun. The LEED gun beam profile was nearly parallel and produced a spot of less than 1 mm diam. The electrons, which were scattered at the Au foil, were measured on the front of the first channel plate, CP_1 in Fig. 7, which was biased at + 100 V. No change in normalized current was measured as the bias on CP_1 was changed from + 100 V to + 300 V. Results of these measurements are shown in Figs. 8(a) and 8(b).

In Fig. 8(a), the normalized current for the G_1 potential of 0 V, and a variety of *Cu* and G_2 bias potentials are shown. In Fig. 8(b), the G_1 bias potential has been increased to

TABLE III. Comparison of the z component of the electron energy for the present design and the old low-energy diffuse scattering polarimeter as implemented for better energy filtering.

θ_0(deg)	E_z(eV):Ref. 14	E_z(eV):here
30°	73	107
40°	48	109
50°	22	107
60°	0	94
65°	0	80
68°	0	53

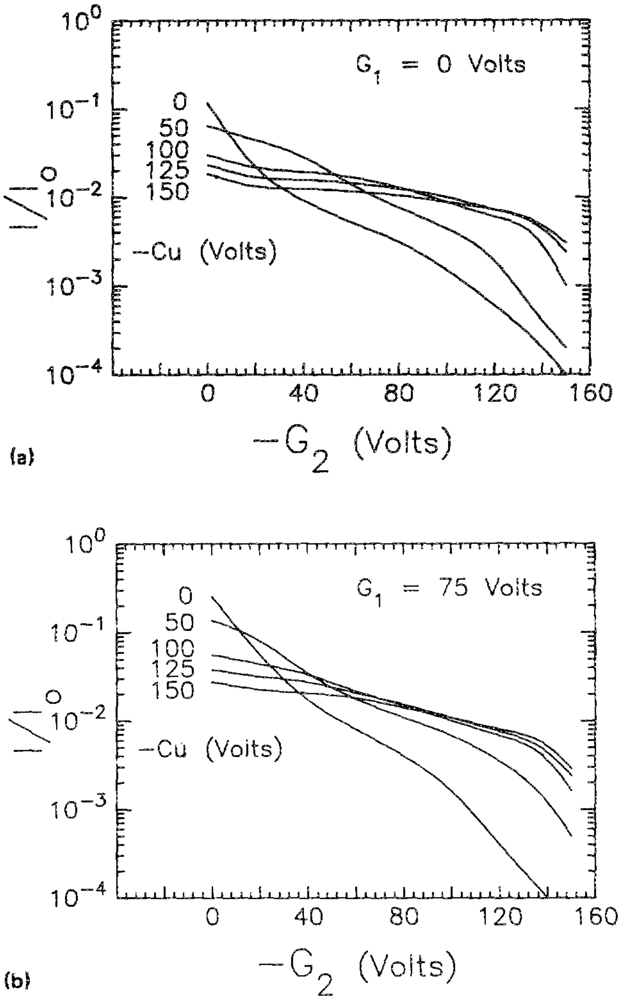

FIG. 8. (a) Normalized current to two quadrants as a function of retarding grid G_2 and shaped electrode Cu potentials for a G_1 potential of 0 V. (b) Normalized current to two quadrants as a function of retarding grid G_2 and shaped electrode Cu potentials for a G_1 potential of 75 V.

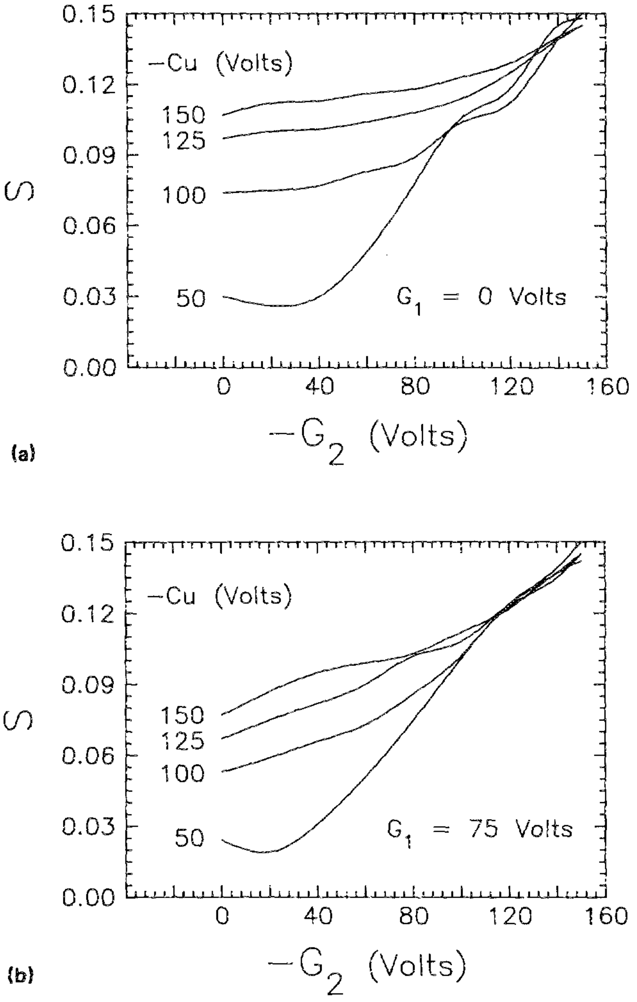

FIG. 9. (a) Effective Sherman function as a function of retarding grid G_2 and shaped electrode Cu potentials for a G_1 potential of 0 V. (b) Effective Sherman function as a function of retarding grid G_2 and shaped electrode Cu potentials for a G_1 potential of 75 V.

+ 75 V. For both values of G_1, as the *Cu* retarding potential is increased, significantly more elastically (quasielastically) scattered electrons are detected over a wide range of G_2 potentials. Further, as the *Cu* retarding potential is increased, fewer lower-energy secondaries (with $S = 0$) are being detected. Also, it is evident that, at higher retarding potentials on G_2, the collection efficiency has been increased by an order of magnitude or more by the shaped Cu electrode.

To measure the Sherman function, a polarized beam of electrons created by irradiating a negative electron affinity (NEA) O:Cs GaAs crystal with circularly polarized light[26] was focused onto the Au foil in the detector. Since the polarization of the beam could be modulated easily, the Sherman function for each detector quadrant could be measured independently[3] and the Sherman function for the detector determined directly. Only 150 eV beams were considered. Once again, a range of operating parameters was surveyed, and the results are given in Fig. 9.

In Figure 9(a) the Sherman function is shown for $G_1 = 0$ V, for a variety of *Cu* electrode and retarding grid G_2 potentials. It is clear that increasing the *Cu* retarding bias increases the Sherman function for the detector. This occurs as a result of two independent phenomena. As *Cu* becomes more negative, more high-angle elastic electrons are detected, and these electrons have a high-scattering asymmetry. Also, as the *Cu* potential is made more negative, fewer secondaries and high-loss inelastically scattered electrons reach the channel plates due to the retarding field near the Au foil caused by the *Cu* electrode and the drift tube. The secondaries carry no real asymmetry information and hence only degrade the detector Sherman function. Thus, the energy prefiltering done by the Cu electrode increases the performance of the detector. In Fig. 9(b), the first grid potential, G_1, is + 75 V. When G_1 is positively biased, the fields are changed, specifically in the region near the drift tube. More inelastically scattered electrons reach the channel plates and degrade the Sherman function for low retarding potentials on G_2. For both values of G_1, the Sherman function reaches a maximum of 0.15 for large retarding potentials on G_2. The measured value of the effective Sherman function for the detector was repeatable day to day with an accuracy of ± 0.005 over the full range of potentials on G_1 and *Cu*.

The FOM for the detector is plotted in Fig. 10(a) for $G_1 = 0$ V, and in Fig. 10(b) for $G_1 =$ + 75 V. It is clear that

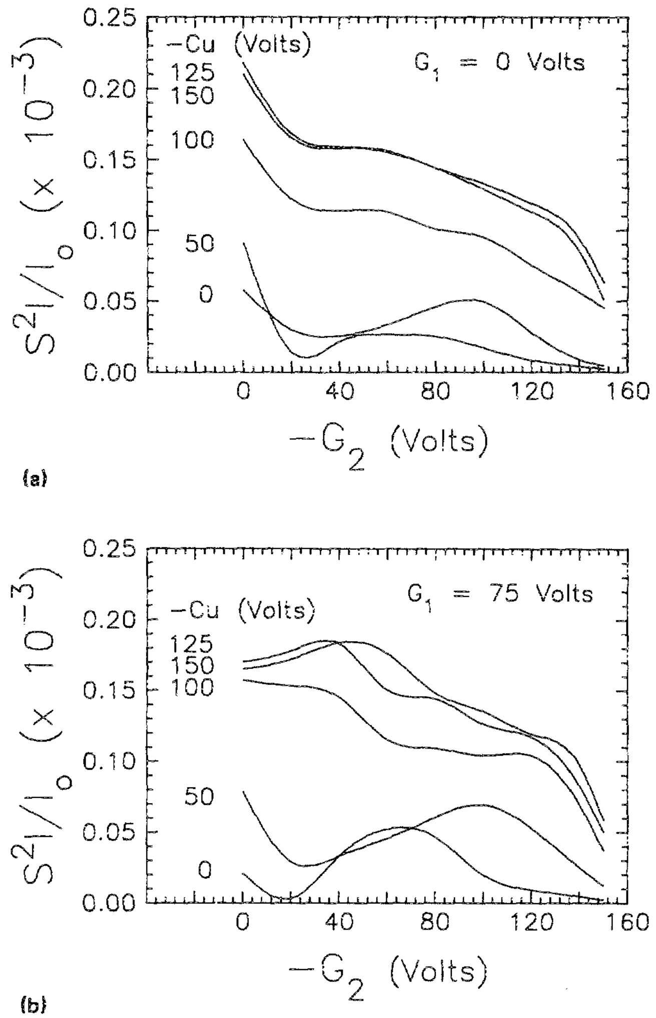

FIG. 10. (a) Figure of merit as a function of retarding grid G_2 and shaped electrode Cu potentials for a G_1 potential of 0 V. (b) Figure of merit as a function of retarding grid G_2 and shaped electrode Cu potentials for a G_1 potential of 75 V.

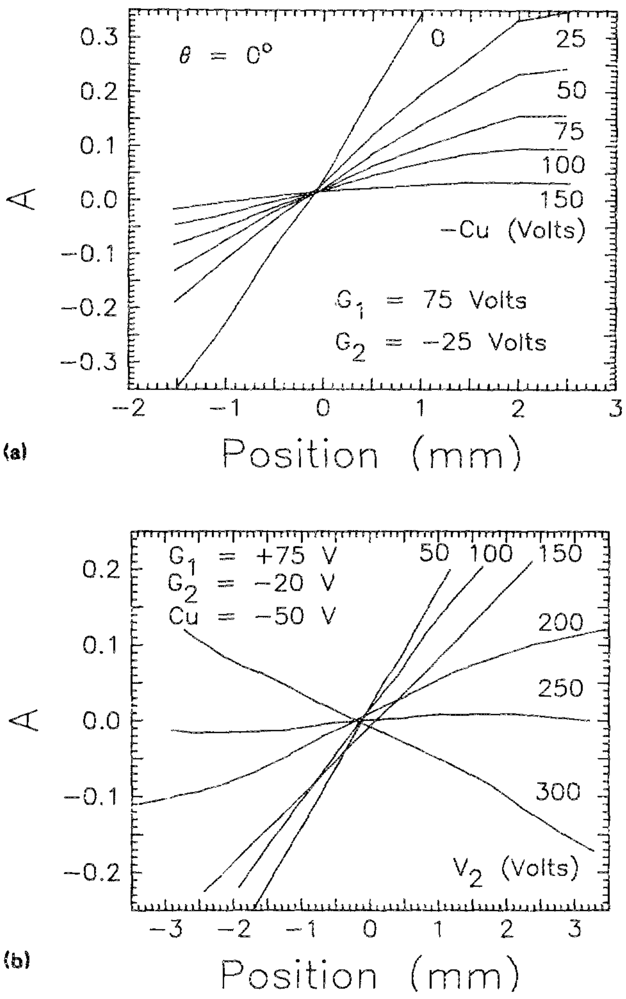

FIG. 11. (a) Displacement asymmetry measured for a variety of Cu electrode potentials at $G_1 = 75$ V and $G_2 = -25$ V. (b) Displacement asymmetry for a variety of V_2 potentials of the einzel lens illustrating the compensation of angular and displacement asymmetries.

the detector should be operated with *Cu* biased in the range $-125 \geqslant Cu \geqslant -150$ V. In this regime, many large-angle elastically scattered electrons reach the channel plates. The most stable operating region appears to be the following: $G_1 = 75$ V, $-50 \leqslant G_2 \leqslant -30$ V and $-150 \leqslant Cu \leqslant -125$ V. In this regime, the FOM $\sim 2.0 \times 10^{-4}$ and $0.09 \leqslant S \leqslant 0.12$ depending upon the specific voltages selected. Under identical operating conditions, we found that the FOM was measured to be the same from day to day to better than ± 5.0%.

B. Instrumental asymmetry compensation

The instrumental asymmetry was measured using a LEED gun mounted on an $\hat{x}$-$\hat{y}$-$\hat{z}$-$\hat{\theta}$ mount. The nearly parallel LEED beam of diameter less than 1 mm could be scanned in position and angle along the Au foil in the detector. One such typical scan is shown in Fig. 11(a) where the beam is scanned in position for some fixed angle and the instrumental asymmetry measured (for a variety of operating conditions).

We summarize the results in Table IV where G_1 and G_2 are fixed and *Cu* is varied, and in Table V where G_1 and *Cu* are fixed and G_2 is varied. In all cases the angular instrumental asymmetry was determined to be $A_\theta = 0.06$ per degree. The angular asymmetry was measured by forming a tilt sequence, positioning the LEED beam in the center of the Au foil, and measuring the resulting asymmetry. The nearly constant angular asymmetry is sensible in light of the fact that it is most sensitive to changes in θ_{in}, which is fixed (θ_{in} is determined by the drift tube and not the fields generated by the electrodes).

TABLE IV. Displacement asymmetry as a function of the Cu electrode bias.

$G_1 = 75$ V and $G_2 = -25$ V	
Cu	A(%/mm)
0	25
−25	15
−50	10
−75	7
−100	5

TABLE V. Displacement asymmetry as a function of grid 2 bias.

$G_1 = 75$ V and $Cu = -50$ V	
G_2	A(%/mm)
-0	5
-25	10
-50	13
-75	18
-100	21
-125	55

The compensation technique is illustrated by Fig. 11(b). In this figure, the operating conditions are $G_1 = 75$ V, $G_2 = -20$ V, and $Cu = -50$ V, although the compensation scheme can be accomplished for any operating condition. The detector had an einzel lens before input as shown in Fig. 12. The image side electrode was physically connected to the drift tube and was grounded in this experiment. The input electrode was also held at ground potential. The center electrode potential was varied in order that the compensation condition be reached. As the parallel rays from the LEED gun enter the einzel lens, they are progressively focused more and more strongly as the voltage of the central element is increased. This means that as the potential on the central element is increased, the rays strike the Au foil at larger and larger angles. In Fig. 11(b), the effect of the increase in potential of the central electrode of the einzel lens is seen to decrease the scan asymmetry until $V_2 = 250$ V where there is little remaining asymmetry. If the lens is focused further, then we essentially "go through" the compensation condition and are overcompensating, and the sign on the asymmetry changes.

The electron optical parameters of the input optics have been calculated. To first order the object (H_0) and image (H_i) side principal planes are located at $z = 98$ mm and $z = 113$ mm, respectively. The object (F_0) side and image (F_i) side focal points are located at $z = 155$ mm and $z = 40$ mm, respectively. The object (f_0) and image (f_i) side focal lengths are 66.8 mm and 66.1 mm, respectively. Based on these electron optical properties of the lenses, we determined that the compensation condition corresponds to 0.71 mm/degree at the Au foil. Referring to Table V, we see that the displacement asymmetry was approximately 10% for $G_2 = -25$ V. Since $A_\theta \sim 6\%$, this corresponds to about 0.6 mm/degree at $G_2 = -25$ V. The compensation technique turns out to be a much more sensitive way to measure the instrumental asymmetries, and the compensation was carried out at a slightly different G_2 potential than the comparison made above. Measurements of compensation for scan asymmetry have been made where the displacement asymmetry can be compensated to better than $A_I = 0.0035$/mm over 4 mm scanning areas. This has the following implications: In a SEMPA experiment, the maximum beam scanning displacement rarely exceeds 100 μm, and thus the error in the measured polarization for this detector ($S \sim 0.10$) would be less than 0.3% for a transport optics magnification of 1.

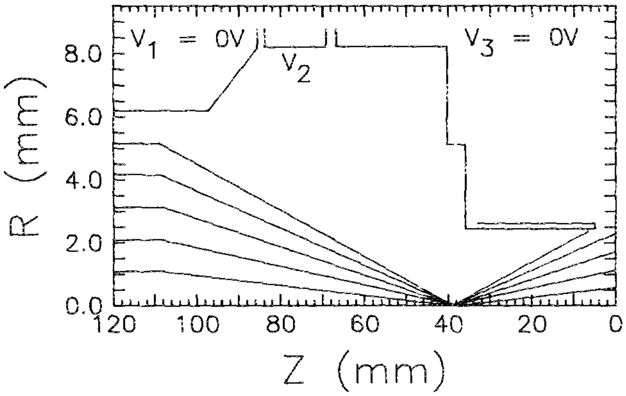

FIG. 12. Cross section of the input einzel lens to the detector with relevant rays shown for excitation of the lens $V_2 = 250$ V.

Once the instrumental asymmetry parameters have been determined, and an experimental set of operating conditions specified (maximum beam or angle movement, etc.), then the mappings of Fig. 6 can be performed with suitably designed transport optics to minimize the instrumental asymmetry.

The low-energy diffuse scattering spin-polarization detector[14] has been redesigned to minimize the instrumental (scan) asymmetry. The instrumental asymmetry has been reduced suitably with a compensation technique. Further, the detector has a FOM of $\sim 2 \times 10^{-4}$, larger than any other polarization detector available. To modify the first version of the low-energy diffuse scattering polarization detector to increase its performance: (1) increase the z distance from the first grid G_1 to the Au foil from 5 to 22.5 mm; (2) increase the drift tube length by 17.5 mm such that the bottom of the snout is 5 mm from the Au target; and (3) add the shaped Cu electrode as shown in Fig. 7. Optimum operation can be achieved when: (1) Au target and drift tube are at the beam potential (i.e., the beam enters the detector in drift space); (2) the potential on the Cu electrode is -150 V relative to the Au target; (3) the potential on the first grid is $+75$ V relative to the Au target; and (4) the potential on the second grid is -60 V relative to the Au target. In this regime, the FOM is $\sim 2.0 \times 10^{-4}$ and the Sherman function ~ 0.10.

ACKNOWLEDGMENT

This work was supported in part by the Office of Naval Research.

[1] R. J. Celotta and D. T. Pierce, Science **234**, 249 (1986).
[2] G. G. Hembree, J. Unguris, R. J. Celotta, and D. T. Pierce, Scanning Microsc. Suppl. **1**, 229 (1987).
[3] J. Kessler, *Polarized Electrons* (Springer, Berlin, 1985).
[4] J. Van Klinken, Nucl. Phys. **75**, 161 (1966).
[5] S. Lin, Phys. Rev. **133**, A965 (1964).
[6] G. Holzwarth and H. J. Meister, Nucl. Phys. **59**, 56 (1964).
[7] L. A. Hodge, T. J. Moravec, F. B. Dunning, and G. K. Walters, Rev. Sci. Instrum. **50**, 5 (1979).
[8] L. G. Gray, M. W. Hart, F. B. Dunning, and G. K. Walters, Rev. Sci. Instrum. **55**, 88 (1984).
[9] F. B. Dunning, L. G. Gray, J. M. Ratliff, F.-C. Tang, X. Zhang, and G. K. Walters, Rev. Sci. Instrum. **58**, 1706 (1987).

[10] J. Kirschner and R. Feder, Phys. Rev. Lett. **42**, 1008 (1979).

[11] J. Kirschner, *Polarized Electrons at Surfaces* (Springer, Berlin, 1985).

[12] D. T. Pierce, S. M. Girvin, J. Unguris, and R. J. Celotta, Rev. Sci. Instrum. **52**, 1437 (1981).

[13] K. Jost, F. Kaussen, and J. Kessler, J. Phys. E **14**, 735 (1981).

[14] J. Unguris, D. T. Pierce, and R. J. Celotta, Rev. Sci. Instrum. **57**, 1314 (1986).

[15] D. T. Pierce, R. J. Celotta, M. H. Kelley, and J. Unguris, Nucl. Instrum. Methods **A256**, 550 (1988).

[16] A. Gellrich, K. Jost, and J. Kessler, in *Proceedings of the 15th International Conference on the Physics of Electron and Atom Collisions* (Brighton, U.K., 1987), p. 818.

[17] M. Fink and A. C. Yates, At. Data **1**, 385 (1970).

[18] M. Fink and J. Ingram, At. Data **4**, 129 (1972).

[19] D. Gregory and M. Fink, At. Nucl. Data **14**, 38 (1974).

[20] J. S. Schilling and M. B. Webb, Phys. Rev. B **2**, 1665 (1970).

[21] M. Landolt (private communication).

[22] L. Reimer, *Scanning Electron Microscopy* (Springer, Berlin, 1985).

[23] K. Jost (private communication).

[24] E. Harting and F. Read, *Electrostatic Lenses* (Elsevier, New York, 1976).

[25] The kernel of the charge density program used was kindly furnished by Dr. E. Kirkland of Cornell University.

[26] D. T. Pierce, R. J. Celotta, G.-C. Wang, W. N. Unertl, A. Galejs, C. E. Kuyatt, and S. R. Mielczarek, Rev. Sci. Instrum. **41**, 478 (1980).